Inductance Interpolation-Based Fast Design and Optimization Methodology for Wireless Power Transfer Systems

Yixiang Yao, Abubakar Uba Ibrahim, *Student Member, IEEE*, and Wenxing Zhong, *Senior Member, IEEE*

***Abstract*—In designing wireless power transfer (WPT) systems, the finite element method (FEM) is usually the interface between the physical entities of the WPT windings and the electrical parameters of the windings such as the inductances and the parasitic resistances. However, this interface is unidirectional, i.e., by knowing the physical parameters of the windings, the electrical parameters can be obtained using the FEM, but not vice-versa. Thus, two challenges are introduced. One is to locate the possible solutions for the physical variables of the windings when the required mutual inductance(s) are determined by the desired characteristics of the WPT system. The other is to search for the optimal solution among the possible ones. Conventionally, the trial-and-error method is adopted to obtain a near-optimal solution, which is time-consuming or even impossible when designing systems with more than two winding-resonators. This article proposes a unique design methodology using the inductance interpolation based approach for WPT systems. With this method, running ONE FEM simulation is sufficient to obtain the required data set for winding design and optimization. The optimization of a three-winding WPT system using the proposed method is provided. The experimental prototype is built, and the measured results are obtained to verify the optimization process.**

***Index Terms*—Fast loss calculation, inductance interpolation, wireless power transfer (WPT).**

NOMENCLATURE

Latin letters

$\boldsymbol{B}$	Magnetic induction.
$\bar{B^2}$	Average value of the square of B.
$(\bar{B_z})^2$	Square of the average B.
$c_{j_a j_b,\kappa_1\kappa_2}$	Interpolation coefficients.
$C(r_a)$	Perimeter of a loop (turn).
D	Diameter of Litz wire.
d	Strand diameter of Litz wire.
f	Operating frequency.
F, G	Factor related to the Litz wire loss.
f_{L_a}	Function about geometry equation of $L_a(r_a)$.
$\boldsymbol{G}(\boldsymbol{x})$	Nonlinear constraint in optimization.
h	Distance between the ferrite and the center of the winding.
$\boldsymbol{H}(\boldsymbol{x})$	Linear inequation constraint in optimization.
$L_a(r_a)$	Path of a-loop.
$\boldsymbol{L}(\boldsymbol{x})$	Linear equation constraint in optimization.
M	Mutual inductance (matrices).
$m(r_a, r_b)$	Mutual inductance function about r_a and r_b.
N_{w}	Number of windings.
P	Power or loss power.
R	Half-width of the outermost turn of a winding.
r	Half-width of an arbitrary turn.
Δr	Spacing of turns.
$S(r_a)$	Area enclosed by a loop (turn).
T	Number of turns of a winding.
$\boldsymbol{x}$	Optimization variable vector.
x, y	Coordinates on xy plane.
z	Distance between the center of the winding and the image winding.

Greek letters

ge	ε rectangle factor, ratio of the length to the width of one winding.
η	Efficiency.
κ_1, κ_2	Degree in spline interpolation.
μ	Vacuum permeability.
σ	Square factor, a turn is close to a quadrangle or a circle.
Ψ	Flux linkage.
ω	Angular frequency.
Ω_a	Path of the boundary in Fig. 10 .

Subscripts

0	Target value or constraint value.
a, b	Labels of two different turns.
$b \sim a$	Response at a generated by excitation at b.
cor.	Value corrected by Appendix C.
ds	DC resistance and skin effect.
ep	Outer proximity effect.
i	Sequence of winding in a WPT system.
ip	Inner proximity effect.
j	Sequence of turn in a winding.
n	Parallel to the winding.
pp	Between primary and primary side.

Manuscript received 13 April 2023; revised 6 July 2023; accepted 2 August 2023. Date of publication 7 August 2023; date of current version 22 September 2023. Recommended for publication by Associate Editor A. Safaee. *(Corresponding author: Wenxing Zhong.)*

The authors are with the Institute of Power Electronics, Zhejiang University, Hangzhou 310027, China (e-mail: 12110008@zju.edu.cn; habuuba@zju.edu.cn; wxzhong@zju.edu.cn).

Color versions of one or more figures in this article are available at https://doi.org/10.1109/TPEL.2023.3302800.

Digital Object Identifier 10.1109/TPEL.2023.3302800

ps	Between primary and secondary side.
SS	SS-WPT system.
ss	Between secondary and secondary side.
x	x-direction in xy plane.
y	y-direction in xy plane.
z	Perpendicular to the winding.

I. Introduction

INDUCTIVE WPT has now been commercialized in wireless charging of portable electronics and electric vehicles (EVs). In inductive WPT applications, winding design and optimization are of vital importance to guarantee a high power-transfer efficiency and a high-power density of the whole system. Additionally, previous studies have introduced multicoupling WPT systems that achieve multiple couplings using three or more windings [1], [2], [3], [4], [5], [6], [7], [8], [9], [10], [11], [12], [13], which present superior performance compared with a conventional two-winding WPT system. However, the design complexity of a multicoupling WPT system is significantly increased due to the increased number of mutual inductances. In designing the WPT windings, the inductances including the self inductances and the mutual inductance(s), and the parasitic resistances of the windings are required for loss calculation and efficiency optimization. Ideally, there are two ways to design WPT windings for a specific application, i.e., the pure analytical calculation method, and the finite element method (FEM) simulation.

For the analytical calculation of inductance, there are quite a few studies have been conducted to develop the analytical calculation methods [14], [15], [16], [17], [18], [19], [20]. The analytical model tends to be complicated when the substrates (i.e., the core and the conductive shield) are included. Moreover, analytical calculation methods are typically applied to an ideal commonly winding shapes like circular or rectangular. However, a practical WPT winding shape is likely a rectangle with four fillets and the fillet angles might also be different from the inner turns to the outer turns of the winding. The analytical modeling of a practical winding is tedious if all these details are included for higher accuracy. Analytically calculating the winding ac resistance is also challenging. The ac resistance is dependent on the magnetic field in the windings. Therefore, calculating the magnetic field in windings is essential for calculating the winding ac resistance. However, when the core and the conductive shield are included in a winding, the calculation of the magnetic field becomes complicated or less accurate [21].

Another method of designing WPT windings is the trial-and-error method based on FEM simulations, e.g., in [22] the coupling coefficient can be optimized separately from the windings' quality factors. The major challenge of this approach is to get accurate winding losses from FEM simulations. A method is introduced in [22], [23], and [24], in which the magnetic field information of the coupled windings is obtained from FEM simulations and then used to theoretically calculate the winding losses. Fig. 1(a) illustrates the simple design flowchart of the trial-and-error method based on the FEM simulation. In this figure, the step of the FEM simulation is inside of the iteration,

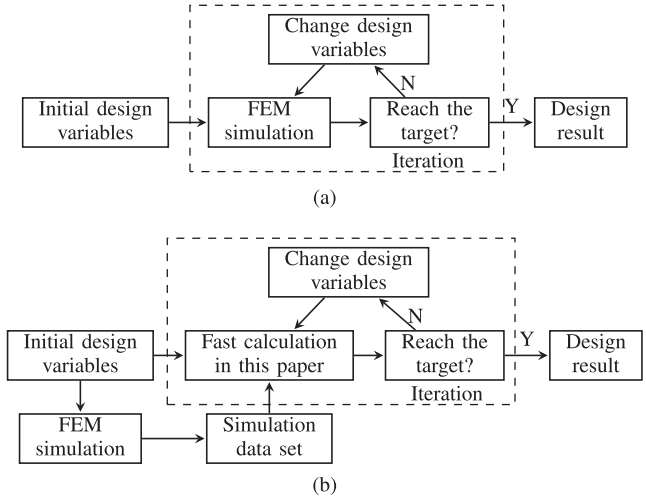

Fig. 1. Design flowchart of (a) trial-and-error method with FEM simulations in each iteration, and (b) fast design and optimization methodology in this article with running FEM simulation ONE time only.

which means that the simulation may need to be run many times during the design process. Furthermore, in the case of a multicoupling WPT system, a higher number of mutual inductances needed to be considered in the design, resulting in a significant increase in the number of required iterations. Therefore, the trial-and-error method is usually time-consuming, especially for multicoupling WPT systems.

To overcome the complication and accuracy issue of the pure analytical calculation method, and also the inefficiency of winding optimization using the trial-and-error method based on a lot of FEM simulations, an inductance interpolation and derivation-based fast design methodology for WPT systems with ferrite plates is proposed in this article. Fig. 1(b) illustrates the design flowchart of this methodology, in which the step of FEM simulation is outside of the iteration. The proposed methodology includes three parts which are explained as follows.

1) An inductance interpolation method is proposed to obtain the continuous inductance functions via the results of the ONE FEM simulation.
2) Based on the continuous inductance functions, a method to locate a possible winding design for achieving the required inductances is proposed. It might not be a serious challenge for a two-winding system to determine the winding parameters after the mutual inductance is given, for example, by using the method proposed in [22]. However, it turns out to be a really troublesome issue when it comes to WPT systems with more than two windings. There will be at least three mutual inductances and a lot more winding variables to be determined. The proposed design method provides a solution to this problem for the first time, as illustrated in the design example given in Section V.
3) Also based on the continuous inductance functions, a winding optimization method is proposed.

Therefore, compared with those design and optimization methods adopted in prior works, the significance of the proposed

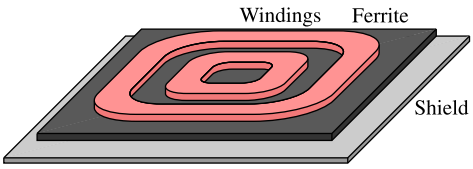

Fig. 2. Pad structure of a WPT system.

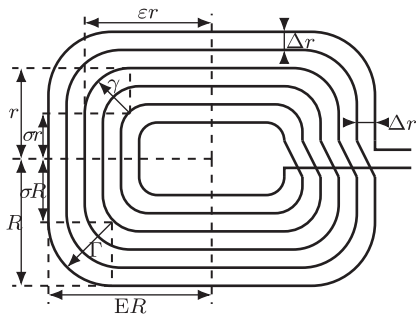

Fig. 3. Geometric model of the winding in WPT systems.

method is that needs only ONE finite-element simulation which makes the design and optimization much more time-efficient.

The rest of this article is organized as follows. Sections II and III introduce two theories, namely, inductance interpolation theory and fast loss calculation theory, respectively. The fast design and optimization methodology are demonstrated in detail in Section IV. In Section V, three-winding WPT systems are designed following this methodology as examples. Based on the first example system, the experimental prototype is built for experimental verification. Finally, Section VI concludes this article.

II. Inductance Interpolation Theory

A. Winding Model

Fig. 2 illustrates the structure of a winding pad with two concentric windings. The number of windings of a pad could be one or more. For cases with more than one winding, concentric arrangement of the windings which means the windings of the same pad share the same normal axes is adopted, as shown in Fig. 2. The pad usually consists of the winding layer, the ferrite layer, and the conductive shielding layer. Fig. 3 illustrates the geometric model of a winding which can be regarded as the combination of straight wires with different lengths and arc wires with different radii. In Fig. 3, r represents half of the width of an arbitrary turn which is termed half-width (r) in the rest of this article, R is the half-width of the outermost turn, γ is the radius of the fillet of an arbitrary turn, Γ is the radius of the fillet of the outermost turn, Δr is the spacing of turns, and t is the number of turns. Here, a square factor σ is defined as

$$\sigma = 1 - \frac{\gamma}{r} \tag{1}$$

σ indicates how much a turn is close to a quadrangle or a circle. For example, $\sigma = 1$ means the radius of the fillet is zero and the turn is a quadrangle (either a square or a rectangle), and on the other hand, $\sigma = 0$ (means the radius of the fillet equals the half-width (r) of the turn), then the square turn becomes a circle. In this study, σ is identical for all turns of a winding. Another factor ε is defined as the ratio of the length to the width of one winding, which is termed rectangle factor. Thereby, the shape of a winding turn can be described with its half-width (r), square factor (σ), and rectangle factor (ε).

B. Obtaining Continuous Mutual Inductance Function Through Interpolation

Continuous mutual inductance function $m(r_a, r_b)$ is defined as the mutual inductance between two arbitrary current loops with half-widths of r_a and r_b, respectively. With this continuous function, the self inductance of any given winding can be calculated by summing the mutual inductance of every two turns of the winding. Similarly, the mutual inductance between any two given windings can be also calculated by summing the mutual inductance of every two turns from two different windings. The calculation formula is given by

$$M_{i_1 i_2} = \sum_{j_1=1}^{T_{i1}} \sum_{j_2=1}^{T_{i2}} m(r_{j_1}, r_{j_2}) \tag{2}$$

where $M_{i_1 i_2}$ is the mutual inductance between winding-i_1 and winding-i_2, m is the continuous mutual inductance function, T_{i1} and T_{i2} are the numbers of turns of the windings, j_1 or j_2 denotes a turn in each of the two windings, and r_{j_1} and r_{j2} are the half-widths (r) of these turns. If winding-i_1 and winding-i_2 refer to the same winding, (2) calculates the self inductance of that particular winding.

Therefore, if the continuous mutual inductance function $m(r_a, r_b)$ is available, the self or mutual inductance of any arbitrary winding(s) with different outer and inner sizes and different number(s) of turns can be theoretically calculated. This will eliminate the large amount of FEM simulations in the winding design process, which will be discussed in detail in Section IV.

For windings without cores and shields, the continuous mutual inductance function $m(r_a, r_b)$ can be theoretically derived. However, for windings with cores and shields, it is hardly possible to theoretically derive the analytical expression of $m(r_a, r_b)$. Therefore, an interpolation-based method is proposed as follows to obtain $m(r_a, r_b)$.

First, an FEM simulation model of a pair of pads can be established for a specified WPT application, as shown in Fig. 4(a). Most of the parameters of this model are given by the application, such as the size of the ferrite, the size of the shield, the maximal outer and minimal inner sizes of the windings, the gap and misalignment of two pads. In this model, arbitrary numbers of turns could be used for two windings as long as the windings occupy the largest allowable areas given by the application. Then, run the FEM simulation and obtain the self inductance of each turn and the mutual inductance between every two turns. Use M_{pp} to denote the inductance matrix consisting of the mutual inductances between every two turns in the primary winding, and similarly, M_{ss} to denote the inductance matrix

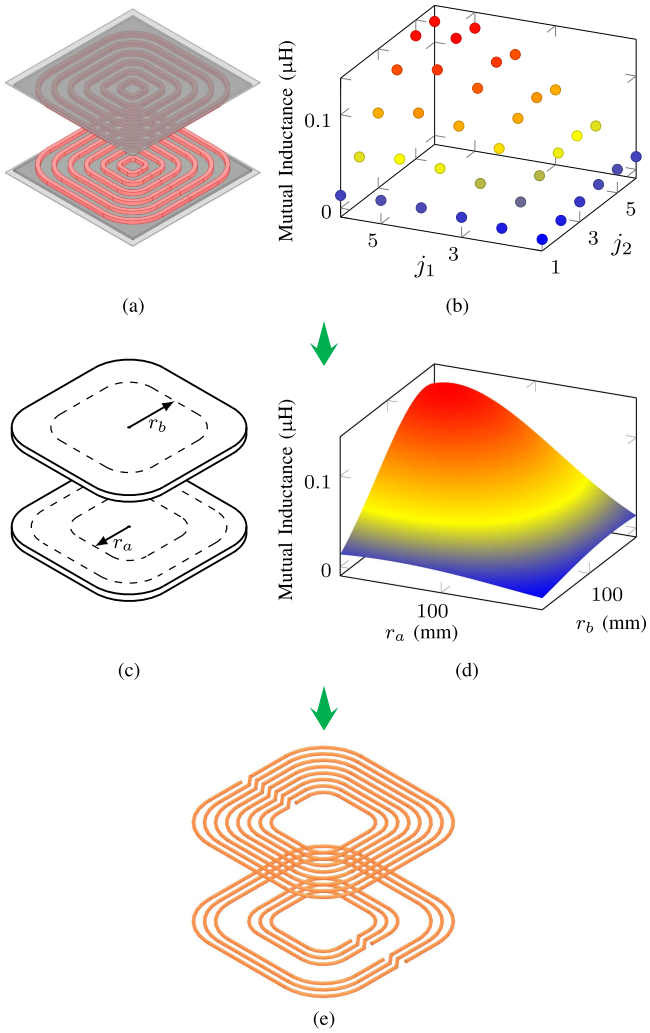

Fig. 4. Inductance interpolation based winding design method. (a) FEM simulation model with arbitrary number of turns. (b) Mutual inductance matrix obtained from FEM simulation. (c) Definition of continuous inductance function. (d) Continuous inductance function obtained by applying interpolation to the mutual inductance matrix. (e) Final designed winding of a three-winding WPT system.

of the turns in the secondary windings, $M_{\rm ps}$ to denote the inductance matrix of one turn from the primary windings and the other turn from the secondary windings. For example, Fig. 4(b) is the visualization of $M_{\rm ps}$, where j_1 and j_2 represent the sequence of the turns (j_1 or $j_2 = 1$ represents the innermost turn). Next, interpolation is applied to $M_{\rm ps}$, $M_{\rm pp}$ and $M_{\rm ss}$ so that the discrete matrices are turned into continuous mutual inductance functions as $m_{\rm ps}(r_a, r_b)$, $m_{\rm pp}(r_a, r_b)$, and $m_{\rm ss}(r_a, r_b)$. These continuous mutual inductance functions can be used to calculate the mutual inductance between two turns with arbitrary sizes and within the allowable winding areas, as shown in Fig. 4(c). In this article, bicubic spline interpolation [25], [26] is adopted. The expression of the bicubic spline interpolation is given by [25]

$$m(r_a, r_b) = \sum_{\kappa_1=0}^{3} \sum_{\kappa_2=0}^{3} c_{j_a j_b, \kappa_1 \kappa_2} (r_a - r_{a,j_a})^{\kappa_1} (r_b - r_{b,j_b})^{\kappa_2} \tag{3}$$

where r_{a,j_a} and r_{b,j_b} are the half-width (r) of the j_ath and j_bth turns, $c_{j_a j_b, \kappa_1 \kappa_2}$ represent the interpolation coefficients when $r_{a,j_a} \le r_a < r_{a,j_a+1}$ and $r_{b,j_b} \le r_b < r_{b,j_b+1}$, which can be calculated with the method present in [25] and [26]. One important characteristic of bicubic spline interpolation is that its first-order, second-order, and mixed partial derivatives are all continuous. Fig. 4(d) visualizes the continuous inductance functions of $m_{\rm ps}(r_a, r_b)$ generated with the interpolation method. With the continuous mutual inductance functions, the parameters of the windings such as the outer and inner sizes, the numbers of turns, etc., can be determined through multiple calculations based on (2) instead of multiple FEM simulations, and thus, a possible design, as shown in Fig. 4(e), can be found efficiently.

III. Fast Losses Calculation Theory

A. Composition of Ohmic Losses in Litz Wire Windings

With an ac current, Litz wire generates three types of losses, i.e., the dc resistance and skin effect loss, denoted as $P_{\rm ds}$; the internal proximity effect loss, denoted as $P_{\rm ip}$; and the external proximity effect loss, denoted as $P_{\rm ep}$ [27], [28], [29]. The formulas for calculating these losses are given by

$$P_{\rm ds} = F_{\rm ds} I^2 \tag{4}$$

$$P_{\rm ip} = G_{\rm ip} I^2 \tag{5}$$

$$P_{\rm ep} = G_{\rm ep} \bar{B}^2 \tag{6}$$

where $F_{\rm ds}$ is a factor of dc resistance and skin effect loss, $G_{\rm ip}$ is a factor related to the inner proximity effect, $G_{\rm ep}$ is a factor related to the outer proximity effect, and $\bar{B}^2$ is the average value of the square of the externally magnetic field in the conductor.

The calculation method of the three factors, $F_{\rm ds}$, $G_{\rm ip}$, and $G_{\rm ep}$, can be found in [28], and the expressions are attached in Appendix A for the complete description of the proposed methodology. The total loss of a winding can be obtained by summing these three losses.

Among these three losses, the former two, i.e., $P_{\rm ds}$ and $P_{\rm ip}$, can be analytically calculated when the geometric parameters of a winding are given. The challenge lies in the calculation of $P_{\rm ep}$ where the information of the magnetic field is required. However, the magnetic field of a winding, as previously explained, cannot be easily and accurately calculated considering the shape of the winding, the ferrite layer and the conductive shield. Conventionally, $\bar{B}^2$ can be obtained by running FEM simulation. Therefore, different winding designs require different FEM simulations, which is time-consuming for system optimization. In the rest of this section, a calculation method for $P_{\rm ep}$ based on the continuous mutual inductance functions is introduced. Thus, only one FEM simulation is needed for winding optimization.

In practice, the actual winding loss will be slightly larger than the theoretically calculated value, because of the increase in strand length due to twisting and broken of strands in the Litz wire, as well as the uneven current distribution due to the nonideal twisting [30], [31], In this study, 10% increment is adopted.

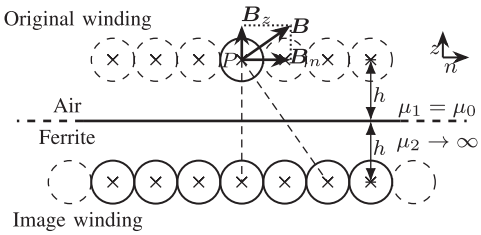

Fig. 5. Source current and image current.

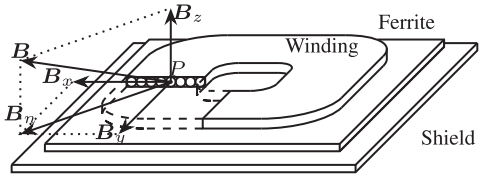

Fig. 6. Magnetic field and its components at point P, where B_z is perpendicular to the winding, B_x and B_y are parallel to the winding, $\boldsymbol{B}_n$ is the resultant field of B_x and B_y.

B. Discussion on the Method of Images

The method of images is usually adopted to calculate the B-field when a ferrite layer exists [32]. Fig. 5 shows the schematic of the source current and the image current in a winding. There are two kinds of media, i.e., air and ferrite, with permeability of μ_1 and μ_2, respectively. The air-ferrite interface is considered infinite. The permeability of the air is usually considered as $\mu_1 = \mu_0$, while μ_2 can be up to thousands times of μ_0, hence μ_2 can be regarded as infinity in the calculation. According to the method of images, the magnetic field in the air can be regarded as the field generated by the original winding and its image winding symmetrical by the air-ferrite interface. Therefore, the larger the ferrite layer, the more accurate the calculation of the B-field based on the method of images. However, the ferrite in a real WPT system has a finite size. Therefore, the method of image is not perfectly precise in this scenario.

To discuss the calculation accuracy, the B-field is decomposed. As shown in Fig. 6, P is the center point of the cross section of a piece of Litz wire in the winding. The distance between P and the air-ferrite interface is h. The magnetic field at point P generated by the current in this piece of wire is zero. In other words, the field at this point is totally external magnetic field. The B-field at this point is decomposed into two components, B_z and $\boldsymbol{B}_n$. B_z is perpendicular to the winding, and $\boldsymbol{B}_n$ is parallel to the winding. $\bar{B}^2$ is given by

$$\bar{B}^2 = \bar{B}_n^2 + \bar{B}_z^2. \tag{7}$$

Simulation studies have been carried out to investigate the accuracy of calculating B_n and B_z with the method of images. Fig. 7(a) shows the simulation model of an actual transmitter. The half-width (r) of the winding, the ferrite and the shield are 175, 200, and 250 mm, respectively. Its counterpart with larger ferrites (three times in x and y dimensions) is shown in Fig. 7(b). The simulation results obtained from the model with larger ferrites are assumed to be close to the calculated

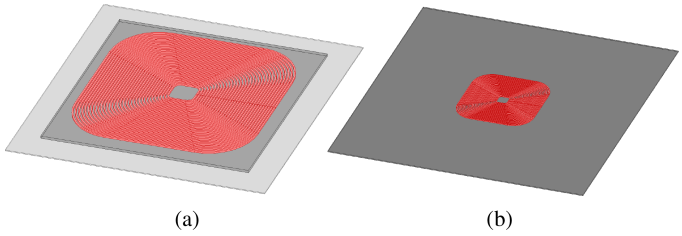

Fig. 7. Simulation models to verify the method of image with (a) normal size ferrite core, (b) ferrite core three times larger than normal size.

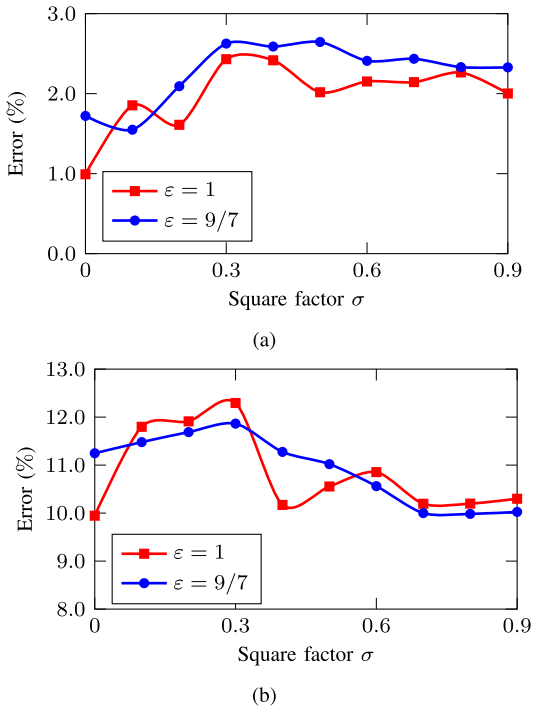

Fig. 8. Error of (a) $\bar{B}_n^2$, (b) $\bar{B}_z^2$, of the simulation results of the system with larger ferrite layers with respect to the simulation results of the actual system, with different square factor σ and different rectangle factor ε of the windings.

results using the method of images. Fig. 8(a) and (b) shows the percentage error of the magnetic field $\bar{B}_n^2$ and $\bar{B}_z^2$, respectively, of the simulation results of the system with larger ferrite layers and that of the actual system, at different σ and different ε. For $\bar{B}_n^2$, the percentage errors are basically less than 3%. However, for $\bar{B}_z^2$, the percentage errors are ranges between 10% and 12%. The reason is explained as follows. At point P, the magnetic field generated by the original winding is always perpendicular to the winding plane. Therefore, B_n is solely generated by the image winding, while B_z is generated by both the original and image windings. Thus, B_n is largely determined by the image current within a small area right blow P due to the short distance between this area and P. The image current in the other area of the image winding contributes little to B_n. Thereby the accuracy of the calculation of B_n based on the method of images is not affected much by the finite size of the ferrite layer. On the other hand, B_z does not share a similar characteristic as B_n and its

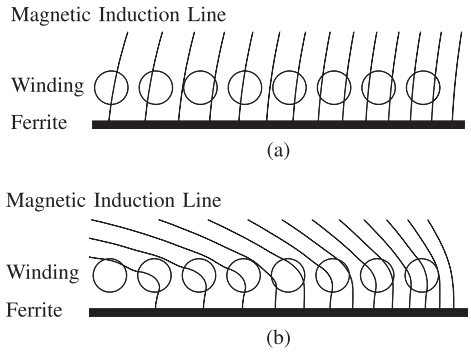

Fig. 9. Magnetic field component generated by, (a) secondary winding(s), and (b) primary winding(s), in the region near the primary ferrite.

calculation is obviously affected by the finite size of the ferrite layer. Therefore, another calculation method for B_z is necessary.

C. Calculation Theory of $\boldsymbol{B}_n$

In the last subsection, the discussion is based on a single winding. However, it should be noted that the B-field that required for loss calculation in (6) is generated by all the windings in the WPT system.

When considering B_n in a particular point of a winding, it is the combination of the fields generated by both the primary windings and the secondary windings. Take calculating B_n on the primary winding as an example. It is found that the magnetic field on the primary winding which is generated by the secondary winding current has negligible B_n component, due to the relatively large distance between two windings and also the large relative permeability of the ferrite. For example, Fig. 9(a) shows the magnetic field lines near the primary ferrite which are generated by the secondary winding current. The filed lines are basically perpendicular to the winding plane. In contrast, the magnetic field generated by the primary winding current has much larger B_n component, as shown in Fig. 9(a). Therefore, when calculating B_n on a winding, only the currents on the same side of the winding are considered. The calculation accuracy is later proved high in Table IV.

The method of images is then used to calculate $\boldsymbol{B}_n$. Fig. 3 demonstrates that each turn in the windings comprises four straight wires and four arc wires. Therefore, to determine the B-field at a specific point induced by the current in this turn, the summation of the B-fields generated by all four straight wires and four arc wires is necessary. This summation can be expressed as

$$\boldsymbol{B}_{n,\text{turn}\sim\text{point}} = \sum_{k_1=1}^{4} \boldsymbol{B}_{n,\text{line-}k_1} + \sum_{k_a=1}^{4} \boldsymbol{B}_{n,\text{arc-}k_a} \tag{8}$$

where $\boldsymbol{B}_{n,\text{line-}l_1}$ and $\boldsymbol{B}_{n,\text{arc-}l_a}$ possess analytical expressions that can be deduced from Appendix B, the symbol "$\sim$" denotes that the current in the turn generates B-field at the point, and similarly hereinafter.

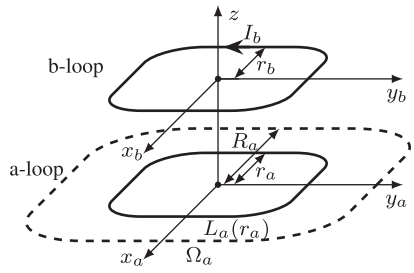

Fig. 10. Mutual inductance between turns in the coil.

The square of B-field at a point generated by all the windings, denoted as $B^2_{n,\text{point}}$, can be calculated by

$$B^2_{n,\text{point}} = \left(\sum_{i'=1}^{N'_w} \sum_{j'=1}^{T'_{i'}} \boldsymbol{B}_{n,\text{turn-}i'j'\sim\text{point}} \right)^2 \tag{9}$$

where N'_w represents the number of windings, and T' represents the number of turns in a winding. $\bar{B}^2_n$ for a winding is obtained by weighted averaging $B^2_{n,\text{point}}$ as follows:

$$\bar{B}^2_{n,\text{winding-}i} = \frac{\sum_{j=1}^{T_i} \int_{\text{turn-}ij} B^2_{n,\text{point}} \mathrm{d}l}{\sum_{j=1}^{T} \int_{\text{turn-}ij} \mathrm{d}l}. \tag{10}$$

D. Calculation Theory of B_z

As previously discussed, B_z cannot be accurately calculated with the method of images. Here a calculation method for B_z is proposed as follows.

Fig. 10 shows two current loops (on the same or different planes), a-loop and b-loop, which are parallel and concentric. The half-widths (r) of the loops are r_a and r_b, the path of a-loop with half-width r_a are denoted as $L_a(r_a)$. The upper limit of r_a is R_a, and the corresponding outermost path is denoted as Ω_a (dashed line in Fig. 10).

When a current I_b is flowing in b-loop, the flux linkage of a-loop $\Psi_{b\sim a}$ is given by

$$\Psi_{b\sim a} = \iint_{S_a(r_a)} B_{z,b\sim a} \mathrm{d}x_a \mathrm{d}y_a \tag{11}$$

where $S_a(r_a)$ is the area enclosed by $L_a(r_a)$; and B_{bz} is the magnetic flux density generated by b-loop and perpendicularly penetrating $S_a(r_a)$.

The coarea formula [33] is used to transform the double integral in (11) to the first type of line integral as

$$\Psi_{b\sim a} = \int_0^{r_a} \mathrm{d}r_a \int_{L_a(r_a)} \frac{B_{z,b\sim a}}{\| \nabla f_{L_a}(x_a, y_a) \|} \mathrm{d}s \tag{12}$$

where $f_{L_a}(x_a, y_a)$ satisfies the geometry equation of $L_a(r_a)$ as follows:

$$f_{L_a}(x_a, y_a) = r_a. \tag{13}$$

Take the derivative of both sides of (12) with respect to r_a, then

$$\frac{\mathrm{d}\,\Psi_{b\sim a}}{\mathrm{d}r_a} = \int_{L_a(r_a)} \frac{B_{z,b\sim a}}{\| \bigtriangledown f_{L_a}(x_a, y_a)\|} \mathrm{d}s. \tag{14}$$

According to the definition of mutual inductance, the mutual inductance between a-loop and b-loop is

$$m(r_a, r_b) = \frac{\Psi_{b\sim a}}{I_b}. \tag{15}$$

Therefore

$$I_b \frac{\partial m(r_a, r_b)}{\partial r_a} = \int_{L_a(r_a)} \frac{B_{z,b\sim a}}{\| \bigtriangledown f_{L_a}(x_a, y_a)\|} \mathrm{d}s. \tag{16}$$

In this study, the gap between any two neighboring turns is unchanged along the wires of the turns. Therefore, according to [34], signed distance function (SDF) can be used to describe $f_{L_a}(x_a, y_a)$, i.e.,

$$\text{SDF} = R_a - f_{L_a}(x_a, y_a). \tag{17}$$

From [34], the modulus of the gradient of an SDF is always equal to one. Thus, $\| \bigtriangledown f_{L_a}(x_a, y_a)\| = 1$. The average magnetic flux density $\bar{B}_{z,b\sim a}$ can be obtained as

$$\bar{B}_{z,b\sim a} = \frac{I_b}{C(r_a)} \cdot \frac{\partial m(r_a, r_b)}{\partial r_a} \tag{18}$$

where $C(r_a)$ is the perimeter of a-loop. Equation (18) means that $\bar{B}_{z,b\sim a}$ can be calculated by taking the partial derivative of the mutual inductance function.

The mutual inductance function $m(r_a, r_b)$ is obtained by using the interpolation method as previously presented. Equation (18) can be used to calculate $\bar{B}_{z,b\sim a}$ on a turn of a winding that is generated by any other turn in the same winding or in a different winding. However, to get a total B_z on this turn, B_z generated by the turn itself is also required. Then a derivative problem appears. The explanation of the problem and the method to solve this problem are given as follows.

Fig. 11(a) shows the graph of the mutual inductance matrix M_{pp}. Take a cross section of Fig. 11(a), as shown in Fig. 11(c), where r_a is variable and r_b is constant. From Fig. 11(c), it can be seen from the trend that the mutual inductance function is nonderivable while $r_a = r_b$. If interpolation is used for the entire domain $[r_{a,\min}, r_{a,\max}]$, as shown in Fig. 11(d), the function will be rounded at $r_a = r_b$, which is not in line with the actual situation. If interpolation is used for the domain $[r_{a,\min}, r_b]$ and $[r_b, r_{a,\max}]$, respectively, as shown in Fig. 11(e), the function will be nonderivable at $r_a = r_b$. The resultant $m_{\text{pp}}(r_a, r_b)$ after interpolation is visualized in Fig. 11(b). Therefore, (18) cannot be directly used to calculate B_z generated by a turn itself. Instead, B_z at the positions of $L_a(r_{a-})$ and $L_a(r_{a+})$, where r_{a-} and r_{a+} represent the values slightly smaller and larger than r_a, respectively, can be calculated and average for estimating B_z at r_a, i.e.,

$$\bar{B}_{z,b\sim a} = \frac{1}{2} \cdot \frac{I}{C(r_a)} \left[\frac{\partial m(r_{a-}, r_b)}{\partial r_{a-}} + \frac{\partial m(r_{a+}, r_b)}{\partial r_{a+}} \right]. \tag{19}$$

Thus, (18) and (19) provide the basic equations for calculating B_z at a winding, which is generated by any windings.

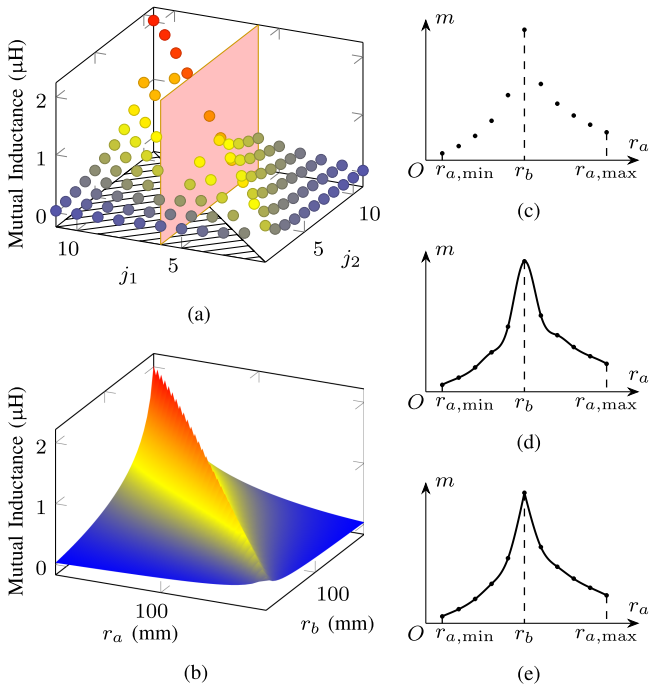

Fig. 11. (a) Graph of the mutual inductance matrix M_{pp}. (b) Graph of the mutual inductance function $m_{\text{pp}}(r_a, r_b)$. (c) Cross section of (a). (d) Use interpolation for $[r_{a,\min}, r_{a,\max}]$. (e) Use interpolation for $[r_{a,\min}, r_b]$ and $[r_b, r_{a,\max}]$, respectively.

It is assumed that the gap between two neighboring turns is constant everywhere. However, a winding with an identical σ for all turns will have different turn-to-turn distances at the fillets from that at the straight area. A method is introduced in Appendix C to correct the error induced by the nonidentical turn-to-turn spacing, from which $\bar{B}_{z,b\sim a}$ can be corrected as follows:

$$\bar{B}_{z,b\sim a,\text{cor.}} \approx \frac{C\,(r_a)}{\frac{\mathrm{d}S(r_a)}{\mathrm{d}r_a}} \bar{B}_{z,b\sim a} \tag{20}$$

where $\bar{B}_{z,b\sim a}$ is calculated by (18) or (19).

Moreover, for the calculation of the external proximity loss P_{ep}, the average of the square B-field (i.e., $\bar{B}_z^2$), is needed, instead of the square of the average B-field $(\bar{B}_z)^2$. However, only $(\bar{B}_z)^2$ can be obtained with (18). Therefore, $(\bar{B}_z)^2$ of a turn is used to approximate $\bar{B}_z^2$, i.e.,

$$(\bar{B}_z)^2 \approx \bar{B}_z^2. \tag{21}$$

Fig. 12 shows the percentage error of $(\bar{B}_z)^2$ with respect to $\bar{B}_z^2$ at different σ factor and ε factor, and the half-width (r) of the winding, the ferrite and the shield are 175, 200, and 250 mm, respectively. It can be seen that the more the winding is close to circular, the less the error is. This is because a circular turn has an evenly distributed B-field and thereby there is no error between $(\bar{B}_z)^2$ and $\bar{B}_z^2$. As shown in Fig. 12, when square factor σ and rectangle factor ε are less than 0.6 and 9/7, respectively, the percentage error is less than 4%. Comparing Fig. 12 with Fig. 8(b), the error of the proposed calculation method is much lower.

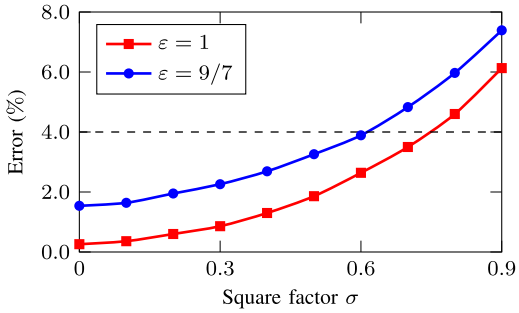

Fig. 12. Error of the calculated $\bar{B}_z^2$ with the proposed method with respect to the FEM simulated at different σ factors and different ε factors of windings.

The average square of B-field for jth turn in ith winding, denoted as $\bar{B}^2_{z,\text{turn-}ij}$, can be calculated by

$$\bar{B}^2_{z,\text{turn-}ij} \approx \left(\sum_{i'=1}^{N'_\text{w}} \sum_{j'=1}^{T'_{i'}} \bar{B}_{z,\text{turn-}i'j'\sim\text{turn-}ij,\text{cor.}} \right)^2 \tag{22}$$

where $\bar{B}_{z,\text{turn-}i'j'\sim\text{turn-}ij,\text{cor.}}$ is $\bar{B}_z$ generated by each turn and is calculated using (20). Then, $\bar{B}_z^2$ for a winding is obtained by weighted averaging $\bar{B}^2_{z,\text{turn-}ij}$ over the length of the turn, i.e.,

$$\bar{B}^2_{z,\text{winding-}i} = \frac{\sum_{j=1}^{T_i} \bar{B}^2_{z,\text{turn-}ij} C_{\text{turn-}ij}}{\sum_{j=1}^{T_i} C_{\text{turn-}ij}} \tag{23}$$

where $C_{\text{turn-}ij}$ is the perimeter of turn-ij.

IV. Design and Optimization Methodology for Windings

According to the basic theory of SS-WPT [35], the required mutual inductance of an SS-WPT system to output a given voltage and power with a given input voltage can be calculated with

$$M_\text{SS} = \frac{U_\text{in} U_\text{out}}{2\pi f P} \tag{24}$$

where U_in and U_out are the input and output ac voltage, respectively, f is the operation frequency, and P is the rated power. In other words, the required mutual inductance can be theoretically calculated to ensure a desired system characteristic. Then, this required mutual inductance can be practically obtained by adjusting the parameters of the windings such as the numbers of turns and the winding sizes. Similarly, it was reported in [1] that the required mutual inductances of a three-winding WPT system can be theoretically calculated to realize a desired misalignment performance.

However, knowing the mutual inductances does not mean a possible winding design can be easily obtained, especially for WPT systems with more than two windings. There are so far no theoretical methods to tell whether a winding design can achieve the desired mutual inductances. To do so, an FEM simulation is usually needed. Therefore, the trial-and-error method which includes a lot of FEM simulations is necessary in searching for a possible design with all the desired mutual inductances. Yet, a solution is not guaranteed, and thus, iterations with different mutual inductances might be required. In this article, a design method based on ONE FEM simulation and the continuous inductance functions is presented.

A. Establish of Simulation Model

First of all, at the beginning of designing a WPT system, the following parameters should be determined according to the actual situation:

1) wire strands and wire diameter D_i of the Litz wire for each winding;
2) square factor σ and rectangle factor ε;
3) the size of the ferrite plates and the shielding plates;
4) the air gap;
5) other geometric parameters required to build the FEM simulation model, such as the clearance between the winding and the ferrite plate, the clearance between the ferrite and the shielding plate, etc.

According to the above configuration, a simulation model is established in the FEM software to acquire the mutual inductance matrices. Using the theory of bicubic spline interpolation, the mutual inductance functions $m_\text{ps}(r_a, r_b)$, $m_\text{ss}(r_a, r_b)$, and $m_\text{pp}(r_a, r_b)$ from the matrices can be derived.

B. Design Method for Windings

Here, N_w is defined as the number of windings in a WPT system. For example, for a WPT system with two windings in the primary side and one winding in the secondary side, N_w is three. For a WPT system with N_w windings, the design method can be described as a mathematical problem in the following way.

1) *Design variables:* Assuming that every spacing of turns (Δr) in the same winding is uniform, to determine a winding, three variables are required, the outer half-width R_i, the inner half-width r_i, and the number of turns T_i. These variables for all the windings form a variable vector $\boldsymbol{x}$, i.e.,

$$\boldsymbol{x} = [R_1, r_1, T_1, \ldots, R_i, r_i, T_i, \ldots, R_{N_\text{w}}, r_{N_\text{w}}, T_{N_\text{w}}]. \tag{25}$$

2) *Constraints:* According to the actual system, set basic linear constraints, such as follows.
   a) For the inner and outer half-widths (r) of the windings, some may be given, and some have to fall in a range, i.e.,

$$\begin{aligned} R_i = R_{i0} \quad &\text{or} \quad R_{i,\min} \le R_i \le R_{i,\max} \\ r_i = r_{i0} \quad &\text{or} \quad r_{i,\min} \le r_i \le r_{i,\max}. \end{aligned} \tag{26}$$

   b) The area of one winding should accommodate its turns, i.e.,

$$R_i - r_i \ge T_i D_i. \tag{27}$$

   These linear conditions can be integrated into a linear equation

$$\boldsymbol{L}([R_1, r_1, T_1, \ldots, R_{N_\text{w}}, r_{N_\text{w}}, T_{N_\text{w}}]) = 0 \tag{28}$$

and a linear inequation

$$\boldsymbol{H}([R_1, r_1, T_1, \ldots, R_{N_\mathrm{w}}, r_{N_\mathrm{w}}, T_{N_\mathrm{w}}]) \leq 0. \quad (29)$$

Moreover, the numbers of turns for windings should be positive integers, i.e.,

$$T_1, \ldots, T_{N_\mathrm{w}} \in \mathbb{N}_+. \quad (30)$$

3) *Design objective:* All the designed mutual inductances should be equal to the given value, i.e.,

$$\begin{aligned}&\boldsymbol{G}([R_1, r_1, T_1, \ldots, R_{N_\mathrm{w}}, r_{N_\mathrm{w}}, T_{N_\mathrm{w}}]) \\ &= \{M_{i_1 i_2}([R_{i_1}, r_{i_1}, T_{i_1}, R_{i_2}, r_{i_2}, T_{i_2}]) - M_{i_1 i_2 0}\} = \{0\}\end{aligned} \quad (31)$$

where $M_{i_1 i_2 0}$ is the targeted mutual inductance between winding-i_1 and winding-i_2.

The mathematical problem can be summarized as

$$\begin{aligned}&\text{solve} \quad \boldsymbol{G}(\boldsymbol{x}) = 0 \\ &\text{s.t.} \quad \boldsymbol{L}(\boldsymbol{x}) = 0, \quad \boldsymbol{H}(\boldsymbol{x}) \leq 0, \quad T_1, \ldots, T_{N_\mathrm{w}} \in \mathbb{N}_+.\end{aligned} \quad (32)$$

The function *fmincon* in MATLAB software can be used to solve this mathematical problem. And linear interpolation method that extends T_i to the field of real numbers and branch and bound method can be used for the integer constraint.

C. Optimization Method for Windings

The winding optimization problem shares a similar model with the winding design problem. The difference is that (31) which is the design objective of the winding design problem, now becomes a nonlinear constraint in the winding optimization problem. The objective of the winding optimization problem is to maximize the power transfer efficiency. The power transfer efficiency can be expressed as follows:

$$\eta([R_1, r_1, T_1, \ldots, R_{N_\mathrm{w}}, r_{N_\mathrm{w}}, T_{N_\mathrm{w}}]) = \frac{P_\mathrm{in} - (P_{L,\mathrm{loss}} + P_{C,\mathrm{loss}})}{P_\mathrm{in}} \quad (33)$$

where P_in is the input power, $P_{L,\mathrm{loss}}$ and $P_{C,\mathrm{loss}}$ are losses in the windings and capacitors, respectively.

According to (4)–(7), (10), and (23), the ohmic loss for a winding can be obtained. After the inductances are calculated with (2), the compensation capacitances can be determined. For example, for a two-winding SS-WPT system, each compensation capacitance is supposed to compensate the reactance of the corresponding winding at the operating frequency, i.e., $C_\mathrm{SS} = 1/(\omega^2 L_\mathrm{SS})$. For the three-winding WPT system in [1], specified calculation formulas for the compensation capacitances were provided. Once the compensation capacitances are determined, the loss caused by the compensating capacitors can be estimated with the following formula, assuming a known quality factor Q_c of the capacitors:

$$P_{C,\mathrm{loss}} = \frac{I_c^2}{\omega Q_c C}. \quad (34)$$

The mathematical problem can be summarized as

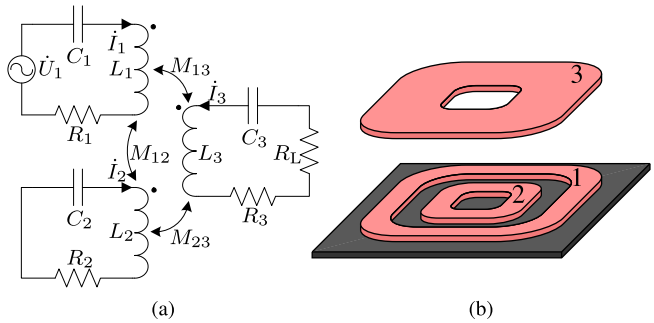

Fig. 13. (a) Simplified circuit model of a three-winding WPT system. (b) Resonant tank structure of the three-winding WPT system (the shields and the upside ferrite are not shown).

$$\begin{aligned}&\max. \quad \eta(\boldsymbol{x}) \\ &\text{s.t.} \quad \begin{cases}\boldsymbol{G}(\boldsymbol{x}) = 0,\ \boldsymbol{L}(\boldsymbol{x}) = 0,\ \boldsymbol{H}(\boldsymbol{x}) \leq 0 \\ T_1, \ldots, T_{N_\mathrm{w}} \in \mathbb{N}_+.\end{cases}\end{aligned} \quad (35)$$

The numerical solution is similar to the previous subsection.

D. Further Optimization for the Spacing of Turns (Δr)

In the above design and optimization, the spacing of turns (Δr) for a winding are uniform, which can be further optimized in this subsection. The previous optimization result has given a group of numbers of turns, namely, $[T_1, \ldots, T_i, \ldots, T_{N_\mathrm{w}}]$, which are needed in this optimization. And then, the variables to be optimized in (32) are the half-width (r) of each turns in the winding group, i.e.,

$$\begin{aligned}\boldsymbol{x} = [\ & r_{11}, \quad \cdots \ r_{1j_1}, \quad \cdots \ r_{1T_1}, \\ & \cdots \\ & r_{i1}, \quad \cdots \ r_{ij_i}, \quad \cdots \ r_{iT_i}, \\ & \cdots \\ & r_{N_\mathrm{w}1}, \ \cdots \ r_{N_\mathrm{w}j_{N_\mathrm{w}}}, \ \cdots \ r_{N_\mathrm{w}T_{N_\mathrm{w}}}].\end{aligned} \quad (36)$$

During the optimization process, some other numbers of turns near $[T_1, \ldots, T_i, \ldots, T_{N_\mathrm{w}}]$ are supposed to be taken and the best result will be chosen.

V. Simulation and Experimental Verification

Three 3.3 kW three-winding WPT systems following the study in [1] are designed using the proposed methodology. These systems are named Example-1, Example-2, and Example-3. Fig. 13(a) shows the simplified circuit model of a three-winding compensated WPT system, where the subscript 1, 2, and 3 represent the transmitter winding (Tx), relay winding (Re), and receiver winding(Rx), respectively. Fig. 13(b) shows the structure of the three-winding coupler. Table I summarizes the physical parameters of the systems. The ferrite plates of the three systems have the same size. Example-1 has a larger shield and a smaller winding. Example-2 and -3 have the same shield and larger windings. In Example-3, the shield and the winding have the same size. Table II summarizes the electrical parameters of the systems. It should be noted that the mutual inductances in Table II are determined to achieve the desired misalignment

TABLE I
PHYSICAL PARAMETERS OF THE THREE-WINDING WPT SYSTEM

Parameters		Value
Quality factor of capacitors Q_c		900
Square factor σ		0.5
Rectangle factor ε		9/7
Airgap		175 mm
Clearance between ferrite and shield		20 mm
Clearance between ferrite and winding		3 mm
Ferrite size		500 mm × 400 mm
Maximum winding size	Example-1	450 mm × 350 mm
	Example-2	480 mm × 380 mm
	Example-3	500 mm × 400 mm
Shield size	Example-1	600 mm × 500 mm
	Example-2	500 mm × 400 mm
	Example-3	500 mm × 400 mm
Litz wire	Strand number	500
	Strand diameter	0.1 mm
	Wire diameter	3.2 mm

TABLE II
ELECTRICAL PARAMETERS OF THE THREE-WINDING WPT SYSTEM

Quantity	Symbol	Value
Output power	P	3.3 kW
Input dc voltage	U_{idc}	400 V
Output dc voltage	U_{odc}	300 V
Transmitter winding current	$I_{\mathrm{Tx,rms}}$	9.64 A
Relay winding current	$I_{\mathrm{Re,rms}}$	9.64 A
Receiver winding current	$I_{\mathrm{Rx,rms}}$	12.22 A
Operation frequency	f	85 kHz
Mutual inductance	M_{12}	40.875 μH
	M_{13}	28.65 μH
	M_{23}	32.27 μH

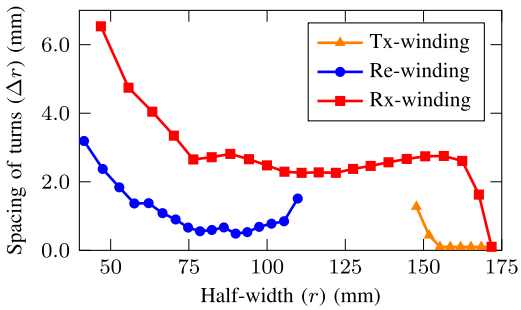

Fig. 14. Spacing of turns (Δr) at different half-widths (r) of the windings of Example-1.

performance. The details of how to determine the mutual inductances are reported in [1].

Following the optimization method in this article, the optimal design of the windings is found. The optimal half-widths (r) of the winding turns are listed in Table III. Fig. 14 depicts the spacing of turns (Δr) of Example-1. As can be seen, the inner spacing is larger than the outer one. This can be attributed to the fact that the B-field is more intense in the inner positions. To mitigate the loss induced by the B-field, the spacing needs to be increased.

TABLE III
OPTIMIZATION RESULTS

(a) Example-1

	Half-width (r) of turns in windings (mm)					
Tx-winding	173.40	170.10	166.80	163.50	160.20	156.90
	153.59	149.96	145.48			
Re-winding	112.15	107.44	103.39	99.41	95.53	91.80
	88.11	84.24	80.44	76.69	72.82	68.72
	64.43	59.86	55.29	50.25	44.68	38.29
Rx-winding	173.40	170.10	165.27	159.46	153.51	147.57
	141.70	135.93	130.27	124.69	119.23	113.76
	108.29	102.80	97.12	91.26	85.25	79.33
	73.48	66.93	59.69	51.75	42.01	

(b) Example-2

	Half-width (r) of turns in windings (mm)					
Tx-Winding	188.40	185.07	181.73	178.35	174.85	171.14
	167.00	161.78	155.46			
Re-Winding	123.86	118.52	113.51	109.05	104.34	99.93
	95.35	90.68	86.38	82.01	77.36	72.34
	67.40	61.81	55.54	49.33	42.38	
Rx-Winding	188.40	181.76	173.83	166.14	159.09	151.83
	144.76	138.00	130.80	124.09	117.56	111.15
	104.41	97.68	90.19	83.05	75.22	66.86
	57.28	45.70				

(c) Example-3

	Half-width (r) of turns in windings (mm)					
Tx-Winding	198.40	195.09	191.69	186.73	181.25	175.49
	169.62	163.61	156.81			
Re-Winding	135.93	129.57	123.72	118.08	112.58	107.09
	101.53	95.84	89.99	84.25	78.46	71.82
	64.70	56.82	47.11			
Rx-Winding	198.40	190.85	182.74	175.12	167.50	160.10
	152.92	145.71	138.78	131.70	124.60	117.69
	110.36	103.27	95.66	88.13	80.03	71.20
	61.38	48.72				

To prove the accuracy of the methodology proposed in this article, three additional FEM simulations are established according to Table III, as shown in Fig. 15. The inductances are calculated using interpolation methods based on simulated data, hence resulting in negligible error between its calculated values and the simulated values. The comparison is shown in Table VI. The B-field values and losses obtained from the proposed methodology are compared with those obtained from the FEM simulations. The details and results of the comparison are given in Table IV. Generally, the external proximity effect loss errors of the three systems are all below 2.5% and are acceptable. Yet, it should be noted that the error of the B-field parallel to the windings (for Example-3) is relatively large. This is because the edge effect has a significant impact on the accuracy of the method of image. When the winding size decreases slightly as in Example-2 and Example-1, the accuracy improves noticeably. Table V lists the comparison of time spent on a single iteration of the trial-and-error method and the proposed method. The numbers of the iterations are the same for both methods to obtain a possible solution. For the proposed method, a single FEM simulation which lasts about 24 min is required before the iteration process, as previously depicted in Fig. 1(b). The

TABLE IV
COMPARISON BETWEEN THE CALCULATION RESULTS AND THE SIMULATION RESULTS OF THE OPTIMAL DESIGN

(a) Example-1

		Simulation	Calculation	Error
		($T^2 \cdot m$)	($T^2 \cdot m$)	
$\int B_n^2 dl$	Tx Winding	1.2295×10^{-5}	1.2493×10^{-5}	1.61%
	Re Winding	1.4890×10^{-5}	1.5466×10^{-5}	3.87%
	Rx Winding	2.4778×10^{-5}	2.5829×10^{-5}	4.24%
$\int B_z^2 dl$	Tx Winding	2.1855×10^{-5}	2.0151×10^{-5}	-7.8%
	Re Winding	5.3206×10^{-5}	5.1687×10^{-5}	-4.44%
	Rx Winding	6.6211×10^{-5}	6.3273×10^{-5}	-2.85%
$\int B^2 dl$	Tx Winding	3.4150×10^{-5}	3.2644×10^{-5}	-4.41%
	Re Winding	6.8096×10^{-5}	6.7153×10^{-5}	-1.38%
	Rx Winding	9.0988×10^{-5}	8.9102×10^{-5}	-2.07%
		(W)	(W)	
Loss	P_{ep}	4.3178	4.2174	-2.33%
	P_{coil}	34.5294	34.429	-0.29%
	P_{total}	77.1464	77.046	-0.13%

(b) Example-2

		Simulation	Calculation	Error
		($T^2 \cdot m$)	($T^2 \cdot m$)	
$\int B_n^2 dl$	Tx Winding	1.0588×10^{-5}	1.1390×10^{-5}	7.57%
	Re Winding	1.1348×10^{-5}	1.1840×10^{-5}	4.34%
	Rx Winding	1.4509×10^{-5}	1.5505×10^{-5}	6.86%
$\int B_z^2 dl$	Tx Winding	2.1852×10^{-5}	2.0172×10^{-5}	-7.69%
	Re Winding	4.1068×10^{-5}	4.0108×10^{-5}	-2.34%
	Rx Winding	4.1613×10^{-5}	3.9934×10^{-5}	-4.03%
$\int B^2 dl$	Tx Winding	3.2440×10^{-5}	3.1562×10^{-5}	-2.71%
	Re Winding	5.2415×10^{-5}	5.1948×10^{-5}	-0.89%
	Rx Winding	5.6122×10^{-5}	5.5439×10^{-5}	-1.22%
		(W)	(W)	
Loss	P_{ep}	3.1475	3.1008	-1.48%
	P_{coil}	32.397	32.352	-0.14%
	P_{total}	69.178	69.132	-0.07%

(c) Example-3

		Simulation	Calculation	Error
		($T^2 \cdot m$)	($T^2 \cdot m$)	
$\int B_n^2 dl$	Tx Winding	6.2596×10^{-6}	8.2550×10^{-6}	31.88%
	Re Winding	7.4449×10^{-6}	7.8428×10^{-6}	5.34%
	Rx Winding	1.3477×10^{-5}	1.5087×10^{-5}	11.94%
$\int B_z^2 dl$	Tx Winding	2.1226×10^{-5}	1.9408×10^{-5}	-8.56%
	Re Winding	2.7856×10^{-5}	2.7270×10^{-5}	-2.10%
	Rx Winding	4.3616×10^{-5}	4.1595×10^{-5}	-4.63%
$\int B^2 dl$	Tx Winding	2.7485×10^{-5}	2.7663×10^{-5}	0.65%
	Re Winding	3.5301×10^{-5}	3.5113×10^{-5}	-0.53%
	Rx Winding	5.7093×10^{-5}	5.6682×10^{-5}	-0.72%
		(W)	(W)	
Loss	P_{ep}	2.6764	2.666	-0.39%
	P_{coil}	32.5678	32.5583	-0.03%
	P_{total}	67.6299	67.6204	-0.01%

TABLE V
COMPARISON OF TIME SPENT AND ITERATION COUNT

	Time spent on a single iteration		Iteration count
	FEA simulation	Fast calculation	
Optimization in Section IV-C	45 min 30 s	0.37 s	434
Optimization in Section IV-D	56 min 4 s	1.02 s	867

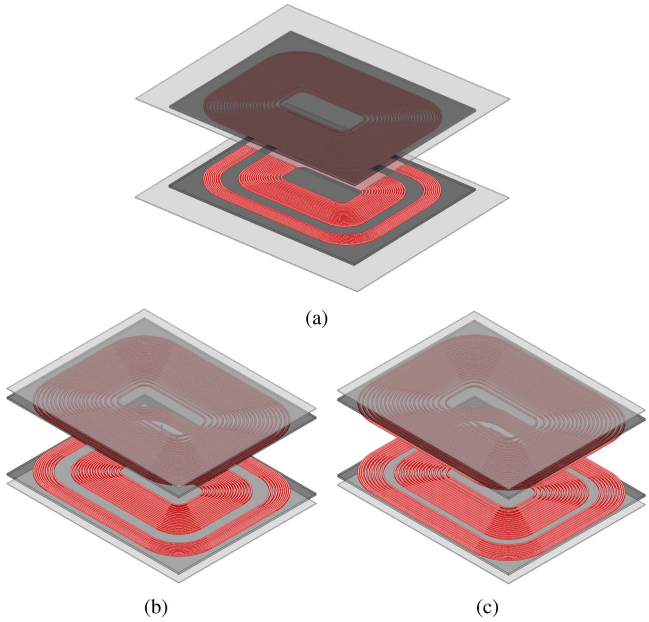

Fig. 15. FEM simulation of the optimized windings of (a) Example-1, (b) Example-2, and (c) Example-3.

TABLE VI
COMPARISON BETWEEN CALCULATION, SIMULATION, AND MEASUREMENT VALUES OF SELF AND MUTUAL INDUCTANCES

(μH)	L_1	L_2	L_3	M_{12}	M_{13}	M_{23}
Calculation	110.26	159.01	289.00	40.87	28.65	32.27
Simulation	110.23	159.10	288.93	40.83	28.54	32.22
Measurement	108.86	157.93	292.61	40.36	28.38	32.62

iteration process of the proposed method for the optimization in Section IV-C roughly takes less than 3 min according to Table V. However, the dominant time spent of the trail-and-error method lies in the iteration process in which several hundreds of iterations are required and each iteration needs more than half an hour. In total, the trial-and-error method needs more than 300 hours to locate a possible solution.

Based on the parameters of Example-1, a three-winding WPT prototype is built as shown in Fig. 16(a). The input voltage of the transmitter is generated by a single-phase full-bridge inverter consisting of four C2M0025120 SiC MOSFETs from Cree. The output full-bridge rectifier consists of four STPS61170CW Schottky Diodes from STMicroelectronics. Fig. 16(b) and (c) shows the transmitter and the receiver windings, respectively. The ferrite cores adopt DMR95 material and the shielding layer is an aluminum plate.

The self inductances and mutual inductances of coils are measured using an *LCR* meter, and the comparison with the calculated values is shown in Table VI, indicating minor differences. The waveforms of the inverter output voltage and current, and the rectifier input voltage and current, are shown in Fig. 17. From the figure, zero-voltage turn-ON of the MOSFETs is realized. A four-channel power analyzer including two high-frequency ac channels is used to measure the losses and efficiency of the system. The measuring points of each channel are shown in

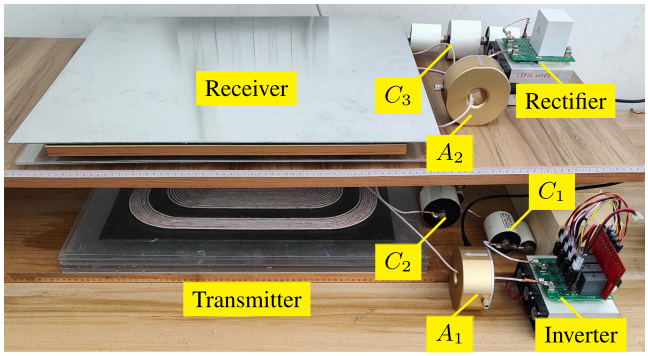

(a)

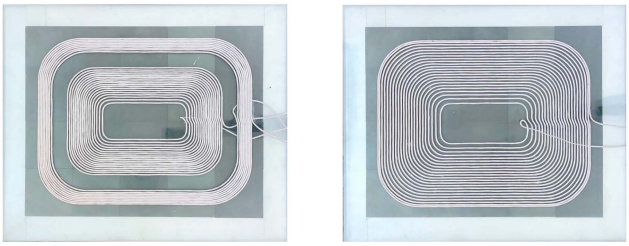

(b) (c)

Fig. 16. (a) Experiment setup of the three-winding WPT system. (b) Transmitter. (c) Receiver.

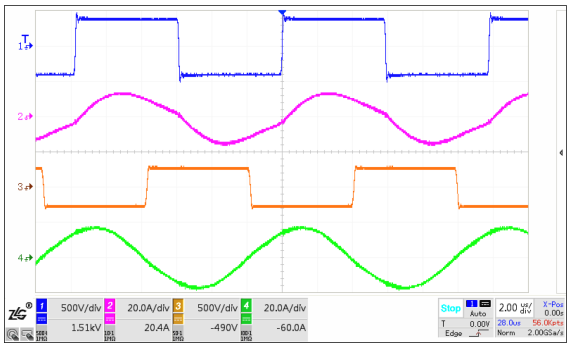

Fig. 17. Waveform of the input voltage (channel-1, blue) and current (channel-2, pink), output voltage (channel-3, orange), and current (channel-4, green).

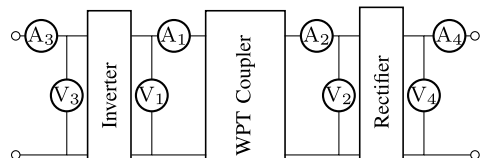

(a)

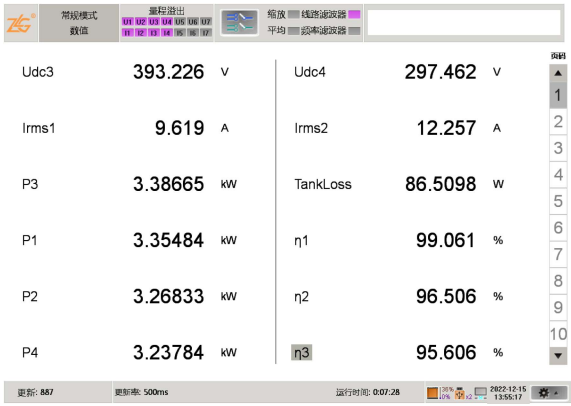

(b)

Fig. 18. (a) Measuring points of current and voltage in the system. (b) Capture of the power analyzer (the subscripts are corresponding to different measuring points).

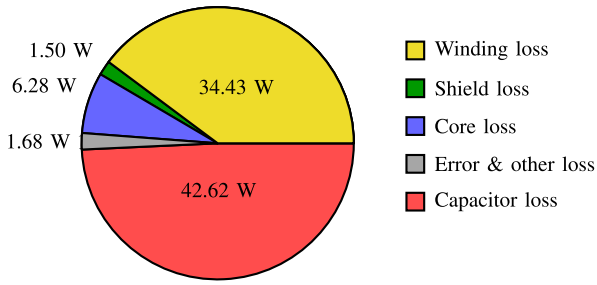

Fig. 19. Pie graph of losses in the resonant tank.

Fig. 18(a). Fig. 18(b) shows the captured screen of the power analyzer. The efficiency of the coupled resonators (i.e., ac to ac) reaches 97.42% and the dc–dc efficiency of the system reaches 95.61% at the air gap of 175 mm. Fig. 19 shows the breakdown of the loss in the system. The core loss and the shield loss (both obtained from FEA simulation) are 6.28 and 1.50 W, respectively. The difference between the total calculated losses and that of the total measured loss is 1.68 W.

Furthermore, the accuracy of the method is validated when considering misalignment situations. Table VII provides an evaluation of the accuracy of the losses calculation by introducing different misalignments in Example-1 along the long side of the pad. The results reveal that the method is equally effective under misalignment conditions.

VI. Conclusion

This article proposes a novel methodology for the design and optimization of magnetic pads in a WPT systems with ferrite plates. The proposed methodology relies on the method of inductance interpolation and derivation, which is more efficient than the normally adopted trial-and-error method, and more accurate than the pure analytical method considering practical factors like winding shape and substrates. The turn-to-turn mutual inductance matrix is first extracted from a single FEM simulation. Then, by applying interpolation to the mutual inductance matrix, a continuous inductance function is obtained. This continuous inductance function can be used to design the windings if mutual inductances are given. By the method of image and taking the derivative of the inductance function, the magnetic field information in the windings is obtained for loss calculation. In this way, the design and optimization of WPT windings require much less FEM simulation than the trial-and-error method and achieve much higher accuracy than the pure analytical method.

TABLE VII
COMPARISON BETWEEN CALCULATION AND SIMULATION VALUES OF MUTUAL INDUCTANCES AND LOSS UNDER MISALIGNMENT CONDITIONS

		Mutual inductance (μH)			Loss (W)	
		M_{12}	M_{13}	M_{23}	P_{ep}	P_{coil}
40 mm	Calculation	40.91	27.63	30.91	4.21	34.48
	Simulation	40.86	27.53	30.86	4.26	34.42
	Error	0.11%	0.37%	0.15%	-1.35%	-0.17%
80 mm	Calculation	41.00	24.80	27.10	4.19	34.40
	Simulation	40.96	24.70	27.06	4.27	34.48
	Error	0.12%	0.39%	0.16%	-1.82%	-0.23%
120 mm	Calculation	41.11	20.683	21.56	4.16	34.37
	Simulation	41.10	20.64	21.55	4.27	34.48
	Error	0.03%	0.20%	0.06%	-2.5%	-0.13%

* The self inductance of windings remains constant with the misalignment.

A prototype three-winding WPT system is designed with the proposed methodology, and the experimental results prove the validity of the methodology.

APPENDIX A

The following is the calculation method of factors of three types of losses according to [27] and [28], where d and D are the strand diameter and total diameter of Litz wire, respectively, ω, μ, and γ are angular frequency, magnetic permeability, and electrical conductivity, respectively, ber_v and bei_v represent the real and imaginary parts of the vth order Kelvin function of the first kind, which is

$$ber_v = ber_v\left(\frac{d\sqrt{\omega\mu r}}{2}\right), \quad bei_v = bei_v\left(\frac{d\sqrt{\omega\mu r}}{2}\right). \tag{37}$$

1) Loss Factor of DC Resistance and Skin Effect:

$$F_{ds} = \frac{1}{\sqrt{2}\pi d}\sqrt{\frac{\omega\mu}{\gamma}}\cdot\frac{ber_0bei_1 - bei_0ber_1 - ber_0ber_1 - bei_0bei_1}{ber_1{}^2 + bei_1{}^2}. \tag{38}$$

2) Loss Factor of Inner Proximity Effect:

$$F_{ip} = \frac{\sqrt{2}d}{2\pi D^2}\sqrt{\frac{\omega\mu}{\gamma}}\cdot\frac{ber_0bei_1 - bei_0ber_1 - ber_0ber_1 - bei_0bei_1}{ber_1{}^2 + bei_1{}^2}. \tag{39}$$

3) Loss Factor of Outer Proximity Effect:

$$G_{ep} = \frac{\sqrt{2}\pi d}{2\mu^2}\sqrt{\frac{\omega\mu}{\gamma}}\cdot\frac{ber_1bei_2 - bei_1ber_2 - ber_1ber_2 - bei_1bei_2}{ber_0{}^2 + bei_0{}^2}. \tag{40}$$

APPENDIX B

1) Straight Wire

For the current in a straight wire, the generated magnetic field $\boldsymbol{B}_n$ at point P is shown in Fig. 20(a). According to the Biot–Savart law, the magnitude of $\boldsymbol{B}_n$ can be calculated with the line integral as follows:

$$B_{n,\text{line}} = \frac{\mu I}{4\pi\sqrt{y^2+z^2}}(\cos\alpha_1 - \cos\alpha_0)\sin\beta. \tag{41}$$

And the direction of $\boldsymbol{B}_n$ is perpendicular to the direction of the straight wire.

2) Arc Wire

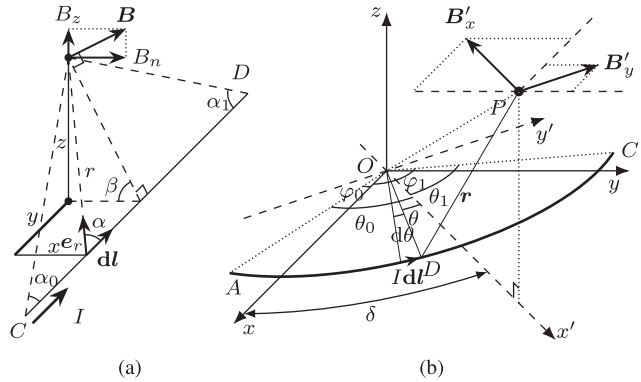

Fig. 20. Magnetic field generated by current in (a) straight wire CD, (b) arc wire $\widehat{AC}$.

For the current in an arc wire, the generated magnetic field B_n at point P is shown in Fig. 20(b). In Fig. 20(b), $Oxyz$ is the Cartesian coordinate system, $\widehat{AC}$ is a circular arc wire on xy plane with the center at O and a radius of R_c, and the current flowing through the arc wire is I. The angle of the starting point A, denoted as $\angle xOA$, equals to φ_0, and the angle of C, i.e., $\angle xOC$, equals to φ_1. P is a point with coordinate of (x, y, z).

To simplify the calculation, the coordinate system is rotated around z axis until P is on xz plane, and the rotation angle is denoted as δ. In this way, a new coordinate system $Ox'y'z$ is created. The new coordinate of P is $(x', 0, z)$, where x' is equal to $\sqrt{x^2+y^2}$. The new angles of the starting and ending points are $\theta_0 = \varphi_0 + \delta$ and $\theta_1 = \varphi_1 - \delta$, respectively.

In the new coordinate system, the current element $I\mathrm{d}\boldsymbol{l}$ at point D on $\widehat{AC}$ is calculated by

$$I\mathrm{d}\boldsymbol{l} = IR_c\left(-\boldsymbol{i}\sin\theta + \boldsymbol{j}\cos\theta\right)\mathrm{d}\theta \tag{42}$$

where θ is the radian of $\angle x'OD$, as shown in Fig. 20(b).

The expression of the vector $\boldsymbol{r}$ from point D to point P is given by

$$\boldsymbol{r} = \boldsymbol{i}\left(x' - R_c\cos\theta\right) - \boldsymbol{j}R_c\sin\theta + \boldsymbol{k}z. \tag{43}$$

According to the Biot–Savart law, the magnetic field components $B_{x'}$ and $B_{y'}$ of x'-direction and y'-direction is

$$\begin{aligned} B_{x'} &= \boldsymbol{i}\cdot\frac{\mu}{4\pi}\int_{\widehat{AC}}\frac{I\mathrm{d}\boldsymbol{l}\times\boldsymbol{r}}{r^3} \\ &= \frac{\mu I}{4\pi}\int_{\widehat{AC}}\frac{R_c z\cos\theta}{\left(R_c^2 + x'^2 + z^2 - 2R_c x'\cos\theta\right)^{3/2}}\mathrm{d}\theta \end{aligned} \tag{44}$$

$$\begin{aligned} B_{y'} &= \boldsymbol{j}\cdot\frac{\mu}{4\pi}\int_{\widehat{AC}}\frac{I\mathrm{d}\boldsymbol{l}\times\boldsymbol{r}}{r^3} \\ &= \frac{\mu I}{4\pi}\int_{\widehat{AC}}\frac{R_c z\sin\theta}{\left(R_c^2 + x'^2 + z^2 - 2R_c x'\cos\theta\right)^{3/2}}\mathrm{d}\theta. \end{aligned} \tag{45}$$

By solving (44), the analytical solution of $B_{x'}$ can be obtained as

$$B_{x'} = B_{x'}(R_c, x', z, \theta_0, \theta_1)$$

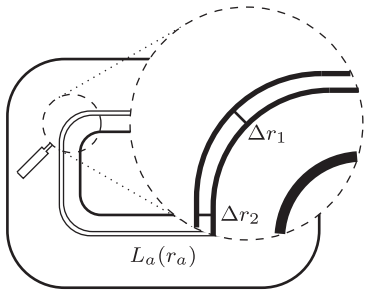

Fig. 21. Inconsistent distance between two turns in a winding, and $\Delta r_1 > \Delta r_2$.

$$= \frac{\mu I z}{8\pi}\sqrt{\frac{-k}{R_c x'^3}}\left\{\frac{k-2}{2\,(k-1)}\left[E\left(\frac{\theta}{2},k\right)-G(\theta,k)\right] - F\left(\frac{\theta}{2},k\right)\right\}\Bigg|_{\theta_0}^{\theta_1} \tag{46}$$

where

$$k=\frac{-4R_c x'}{(R_c-x')^2+z^2},\quad G\,(\theta,k)=\frac{k\sin\theta}{\sqrt{4+2k\,(\cos\theta-1)}}. \tag{47}$$

$F(\phi,k)$ and $E(\phi,k)$ are incomplete elliptic integrals. The method described in [36] and [37] can be used to solve the numerical integration of the elliptic function.

By solving (45), the analytical solution of $B_{y'}$ can be obtained as

$$B_{y'} = B_{y'}(R_c,x',z,\theta_0,\theta_1) = -\frac{\mu I z}{4\pi x}\left(\frac{1}{\sqrt{R_c^2+x'^2+z^2-2R_c x'\cos 2\theta}}\right)\Bigg|_{\theta_0}^{\theta_1}. \tag{48}$$

From (46) and (48), the magnetic field in x' and y' directions in the coordinate system $x'Oy'$ can be calculated by

$$\begin{bmatrix}B_{x'}\\B_{y'}\end{bmatrix} = \begin{bmatrix}B_{x'}(R_c,\sqrt{x_0^2+y_0^2},z,\varphi_0-\delta,\varphi_1-\delta)\\B_{y'}(R_c,\sqrt{x_0^2+y_0^2},z,\varphi_0-\delta,\varphi_1-\delta)\end{bmatrix}. \tag{49}$$

Magnetic field in the original xOy coordinate system can be calculated by rotating $x'Oy'$ back to xOy as

$$\boldsymbol{B}_{n,\text{arc}} = \begin{bmatrix}B_x\\B_y\end{bmatrix} = \begin{bmatrix}\cos\delta & -\sin\delta\\ \sin\delta & \cos\delta\end{bmatrix}\begin{bmatrix}B_{x'}\\B_{y'}\end{bmatrix}. \tag{50}$$

Appendix C
Error Correction

The distance between two turns in a winding is inconsistent, as shown in Fig. 21. Therefore, $\| \bigtriangledown f_{L_a} \| \not\equiv 1$. For (16), according to mean value theorem for integrals [38], there exists a point $(x_{\xi 1}, y_{\xi 1})$ on line $L_a(r_a)$ to make

$$\int_{L_a(r_a)} \frac{B_{z,b\sim a}(x_a,y_a)}{\| \bigtriangledown f_{L_a} \|}\mathrm{d}s = B_{z,b\sim a}(x_{\xi 1},y_{\xi 1})\int_{L_a(r_a)}\frac{1}{\| \bigtriangledown f_{L_a} \|}\mathrm{d}s \tag{51}$$

where $B(x_{\xi 1}, y_{\xi 1})$ is the mean value. And similarly, there exists a point $(x_{\xi 2}, y_{\xi 2})$ on line $L_a(r_a)$ to make

$$\int_{L_a(r_a)} B_{z,b\sim a}(x_a,y_a)\mathrm{d}s = B_{z,b\sim a}(x_{\xi 2},y_{\xi 2})\int_{L_a(r_a)}\mathrm{d}s \tag{52}$$

where $B(x_{\xi 2}, y_{\xi 2})$ is the mean value. Assuming that the above two mean values are approximately equal, then

$$B_{z,b\sim a}(x_{\xi 1},y_{\xi 1}) \approx B_{z,b\sim a}(x_{\xi 2},y_{\xi 2}). \tag{53}$$

Therefore

$$\frac{\int_{L_a(r_a)}\frac{B_{z,b\sim a}}{\| \bigtriangledown f_{L_a} \|}\mathrm{d}s}{\int_{L_a(r_a)}\frac{1}{\| \bigtriangledown f_{L_a} \|}\mathrm{d}s} \approx \frac{\int_{L_a(r_a)} B_{z,b\sim a}\mathrm{d}s}{\int_{L_a(r_a)}\mathrm{d}s}. \tag{54}$$

In (11) and (12), if $B_{z,b\sim a}=1$, and take the derivative of r_a, then

$$\int_{L_a(r_a)}\frac{1}{\| \bigtriangledown f_{L_a} \|}\mathrm{d}s = \frac{\mathrm{d}S(r_a)}{\mathrm{d}r_a} \tag{55}$$

where $S(r_a)$ is the enclosed areas of $L_a(r_a)$. And in addition

$$\int_{L_a(r_a)}\mathrm{d}s = C(r_a) \tag{56}$$

where $C(r_a)$ is the perimeter of $L_a(r_a)$. In this way, with (16) and (54) the correction for the line integral is given by

$$\int_{L_a(r_a)} B_{z,b\sim a}\mathrm{d}s \approx I_b\frac{\partial m(r_a,r_b)}{\partial r_a}\cdot\frac{C(r_a)}{\frac{\mathrm{d}S(r_a)}{\mathrm{d}r_a}}. \tag{57}$$

Therefore, the corrected $\bar{B}_{z,b\sim a}$ can be obtained as

$$\bar{B}_{z,b\sim a} \approx \frac{I_b}{\frac{\mathrm{d}S(r_a)}{\mathrm{d}r_a}}\cdot\frac{\partial m(r_a,r_b)}{\partial r_a}. \tag{58}$$

And compared with the noncorrected $\bar{B}_{z,b\sim a}$ in (18), the corrected $\bar{B}_{z,b\sim a}$ can be calculated as (20).

References

[1] Y. Yao, A. U. Ibrahim, and W. Zhong, "A three-resonator wireless power transfer system with constant-output feature within a misalignment range," *IEEE Trans. Power Electron.*, vol. 37, no. 12, pp. 15753–15763, Dec. 2022.

[2] Q. Zhu, Y. Guo, L. Wang, C. Liao, and F. Li, "Improving the misalignment tolerance of wireless charging system by optimizing the compensate capacitor," *IEEE Trans. Ind. Electron.*, vol. 62, no. 8, pp. 4832–4836, Aug. 2015.

[3] X. Dang, P. Jayathurathnage, S. A. Tretyakov, and C. R. Simovski, "Self-tuning multi-transmitter wireless power transfer to freely positioned receivers," *IEEE Access*, vol. 8, pp. 119940–119950, 2020.

[4] J. Zhang, X. Yuan, C. Wang, and Y. He, "Comparative analysis of two-coil and three-coil structures for wireless power transfer," *IEEE Trans. Power Electron.*, vol. 32, no. 1, pp. 341–352, Jan. 2017.

[5] S. Moon, B.-C. Kim, S.-Y. Cho, C.-H. Ahn, and G.-W. Moon, "Analysis and design of a wireless power transfer system with an intermediate coil for high efficiency," *IEEE Trans. Ind. Electron.*, vol. 61, no. 11, pp. 5861–5870, Nov. 2014.

[6] W. Zhong, C. Zhang, X. Liu, and S. R. Hui, "A methodology for making a three-coil wireless power transfer system more energy efficient than a two-coil counterpart for extended transfer distance," *IEEE Trans. Power Electron.*, vol. 30, no. 2, pp. 933–942, Feb. 2015.

[7] A. Kamineni, G. A. Covic, and J. T. Boys, "Analysis of coplanar intermediate coil structures in inductive power transfer systems," *IEEE Trans. Power Electron.*, vol. 30, no. 11, pp. 6141–6154, Nov. 2015.

[8] Y. Li, Q. Xu, T. Lin, J. Hu, Z. He, and R. Mai, "Analysis and design of load-independent output current or output voltage of a three-coil wireless power transfer system," *IEEE Trans. Transp. Electrific.*, vol. 4, no. 2, pp. 364–375, Jun. 2018.
[9] D. H. Tran et al., "Design of a high-efficiency wireless power transfer system with intermediate coils for the on-board chargers of electric vehicles," *IEEE Trans. Power Electron.*, vol. 33, no. 1, pp. 175–187, Jan. 2018.
[10] P. Darvish, S. Mekhilef, and H. A. B. Illias, "A novel S–S–LCLCC compensation for three-coil WPT to improve misalignment and energy efficiency stiffness of wireless charging system," *IEEE Trans. Power Electron.*, vol. 36, no. 2, pp. 1341–1355, Feb. 2021.
[11] L. Tian, F. Yang, B. Cai, S. Li, K. Liu, and H. Zhao, "High misalignment tolerance in efficiency of WPT system with movable intermediate coil and adjustable frequency," *IEEE Access*, vol. 9, pp. 139527–139535, 2021.
[12] Y. Chen, R. Mai, Y. Zhang, M. Li, and Z. He, "Improving misalignment tolerance for IPT system using a third-coil," *IEEE Trans. Power Electron.*, vol. 34, no. 4, pp. 3009–3013, Apr. 2019.
[13] D. Bui, Q. Zhu, L. Zhao, and A. P. Hu, "Concentric-coil hybrid IPT system with improved tolerance to coupling and load variations," *IEEE Trans. Emerg. Sel. Topics Power Electron.*, vol. 10, no. 4, pp. 4913–4922, Aug. 2022.
[14] F. W. Grover, *Formulas and Tables for the Calculation of the Inductance of Coils of Polygonal Form*, US Department of Commerce, Bureau of Standards, 1923.
[15] H. A. Wheeler, "Inductance formulas for circular and square coils," *Proc. IEEE Proc. IRE*, vol. 70, no. 12, pp. 1449–1450, Dec. 1982.
[16] W. G. Hurley and M. C. Duffy, "Calculation of self-and mutual impedances in planar sandwich inductors," *IEEE Trans. Magn.*, vol. 33, no. 3, pp. 2282–2290, May 1997.
[17] Y. Su, X. Liu, and S. R. Hui, "Mutual inductance calculation of movable planar coils on parallel surfaces," *IEEE Trans. Power Electron.*, vol. 24, no. 4, pp. 1115–1123, Apr. 2009.
[18] B. K. Kushwaha, G. Rituraj, and P. Kumar, "3-D analytical model for computation of mutual inductance for different misalignments with shielding in wireless power transfer system," *IEEE Trans. Transp. Electrific.*, vol. 3, no. 2, pp. 332–342, Jun. 2017.
[19] F. J. López-Alcolea, J. V. del Real, P. Roncero-Sánchez, and A. P. Torres, "Modeling of a magnetic coupler based on single-and double-layered rectangular planar coils with in-plane misalignment for wireless power transfer," *IEEE Trans. Power Electron.*, vol. 35, no. 5, pp. 5102–5121, May 2020.
[20] Z. Luo and X. Wei, "Analysis of square and circular planar spiral coils in wireless power transfer system for electric vehicles," *IEEE Trans. Ind. Electron.*, vol. 65, no. 1, pp. 331–341, Jan. 2018.
[21] M. Lu and K. D. Ngo, "Analytical calculation of proximity-effect resistance for planar coil with Litz wire and ferrite plate in inductive power transfer," *IEEE Trans. Ind. Appl.*, vol. 55, no. 3, pp. 2984–2991, May/Jun. 2019.
[22] R. Bosshard, J. W. Kolar, J. Mühlethaler, I. Stevanović, B. Wunsch, and F. Canales, "Modeling and η - α -Pareto optimization of inductive power transfer coils for electric vehicles," *IEEE Trans. Emerg. Sel. Topics Power Electron.*, vol. 3, no. 1, pp. 50–64, Mar. 2015.
[23] R. Bosshard, "Multi-objective optimization of inductive power transfer systems for EV charging," Ph.D. dissertation, Power Electron. Syst. Lab., ETH Zurich, Zurich, Switzerland, 2015.
[24] J. Mühlethaler, "Modeling and multi-objective optimization of inductive power components," Ph.D. dissertation, ETH Zurich, Zurich, Switzerland, 2012.
[25] C. De Boor, "Bicubic spline interpolation," *J. Math. Phys.*, vol. 41, no. 1–4, pp. 212–218, 1962.
[26] B. Bhattacharyya, "Bicubic spline interpolation as a method for treatment of potential field data," *Geophysics*, vol. 34, no. 3, pp. 402–423, 1969.
[27] J. Lammeraner, M. Štafl, and E. Currents, *International Scientific Series*. Boca Raton, FL, USA: CRC Press, 1966.
[28] J. Ferreira, "Analytical computation of AC resistance of round and rectangular litz wire windings," *IEE Proc. B. Elect. Power Appl.*, vol. 139, pp. 21–25, 1992.
[29] J. A. Ferreira, "Improved analytical modeling of conductive losses in magnetic components," *IEEE Trans. Power Electron.*, vol. 9, no. 1, pp. 127–131, Jan. 1994.
[30] C. R. Sullivan and R. Y. Zhang, "Analytical model for effects of twisting on litz-wire losses," in *Proc. IEEE 15th Workshop Control Model. Power Electron.*, 2014, pp. 1–10.
[31] T. Guillod, J. Huber, F. Krismer, and J. W. Kolar, "Litz wire losses: Effects of twisting imperfections," in *Proc. IEEE 18th Workshop Control Model. Power Electron.*, 2017, pp. 1–8.
[32] J. D. Jackson, *Classical Electrodynamics*. New York: Wiley, 1975.
[33] H. Federer, *Geometric Measure Theory*. Berlin, Germany: Springer, 2014.
[34] Deutsch, *Level Set Methods and Dynamic Implicit Surfaces*. Berlin, Germany: Springer.
[35] W. Zhong, D. Xu, R. S. Y. Hui, D. Xu, and R. S. Y. Hui, *Wireless Power Transfer: Between Distance and Efficiency*. Berlin, Germany: Springer, 2020.
[36] R. Bulirsch, "Numerical calculation of ellipticintegrals and elliptic functions," *Numerische Mathematik*, vol. 7, no. 1, pp. 78–90, 1965.
[37] B. C. Carlson, "Elliptic integrals," *NIST Handbook Math. Functions*, vol. 1, pp. 485–522, 2010.
[38] H. Amann, J. Escher, and G. Brookfield, *Analysis*. Basel, Switzerland: Birkhäuser, 2005.

Yixiang Yao was born in Shanxi Province, China, in 1997. He received the B.Eng. degree in electrical engineering and automation from Xi'an Jiaotong University, Xi'an, China, in 2019. He is currently working toward the Ph.D. degree in electrical engineering with Zhejiang University, Hangzhou, China.

His current research interests include wireless power transfer technologies and power electronics.

Abubakar Uba Ibrahim (Student Member, IEEE) received the B.Eng. degree in electrical engineering from Bayero University Kano, Kano, Nigeria, in 2008, the M.Sc. degree in electronics and electrical engineering from Strathclyde University, Glasgow, U.K., in 2012, and the Ph.D. degree in power electronics from the Department of Electrical and Electronic Engineering, Zhejiang University, Hangzhou, China, in 2021.

He is currently a Postdoctoral Fellow with the Research Institute, Zhejiang University, Taizhou, China. His research interests include wireless power transfer technologies and their driving power converters.

Wenxing Zhong (Senior Member, IEEE) received the B.Eng. degree in electrical engineering from Tsinghua University, Beijing, China, in 2007 and the Ph.D. degree in power electronics from the City University of Hong Kong, Hong Kong, in 2012.

He is currently a Professor with the Department of Electrical Engineering, Zhejiang University, Hangzhou, China. From 2016 to 2017, he was a Research Assistant Professor with the Department of Electrical and Electronic Engineering, University of Hong Kong, Hong Kong. His research interests include wireless power transfer and power electronics.

Dr. Zhong was the recipient of two Transactions First Prize Paper Awards from IEEE Power Electronics Society.